Results from the commissioning of the Gemini South Adaptive Optics Imager (GSAOI) at Gemini South Observatory

Eleazar R. Carrasco[a], Michelle L. Edwards[a], Peter J. McGregor[b], Cláudia Winge[a], Peter J. Young[b], Matthew C. Doolan[b], Jan van Harmelen[b], Francois J. Rigaut[a], Benoit Neichel[a], Gelys Trancho[c], Etienne Artigau[d], Peter Pessev[a], Felipe Colazo[a], Jennifer Tigner[e], Francesco Mauro[f], Javier Lührs[a] and William N. Rambold[a]

[a]Gemini Observatory/AURA, Southern Operations Center, Casilla 603, La Serena, Chile;

[b]Research School of Astronomy and Astrophysics, The Australian National University, Cotter Road, Weston, ACT Australia 2611;

[c]Giant Magellan Telescope Organization, 251 S. Lake Avenue, Pasadena, CA 91001, USA;

[d]Département de Physique and Observatoire du Mont Mégantic, Université de Montréal, C.P. 6128, Succ. Centre-Ville, Montreal, QC H3C 3J7, Canada;

[e] Department of Physics and Astronomy, University of Victoria, PO Box 3055 Stn Csc, Victoria, Canada;

[f] Department of Astronomy, Universidad de Concepción, Casilla 160-C, Concepción, Chile

ABSTRACT

We present the results from the commissioning of the Gemini South Adaptive Optics Imager (GSAOI). Capable of delivering diffraction limited images in the near-infrared, over an $85'' \times 85''$ square field-of-view, GSAOI was designed for use with the Gemini Multi-Conjugate Adaptive Optics (GeMS) system in operation at the Gemini South Observatory. The instrument focal plane, covered by an array of four HAWAII-2RG detectors, contains 4080×4080 pixels and has a plate scale of $0.02''$ – thus capitalizing on the superb image quality delivered by both the all-refractive optical design of GSAOI and the Gemini South MCAO system. Here, we discuss our preliminary findings from the GSAOI commissioning, concentrating on detector characterization, on-sky performance and system throughput. Further specifics about the Gemini MCAO system can be found in other presentations at this conference.

Keywords: near-infrared, instrumentation, instrument commissioning, image, Gemini, adaptive optics system

1. INTRODUCTION

The Gemini telescopes were designed to provide the best image quality with the lowest possible emissivity for optimal infrared observing from the ground for 8-10 m class telescopes. The Gemini Adaptive Optics (AO) program has been of high priority for the observatory since 2000. The success of the AO program at Gemini has been demonstrated elsewhere with the use of ALTAIR, a natural guide star (NGS) and laser guide star (LGS) adaptive optics system at Gemini North, and with different facility instruments such as the Near-Infrared Imager and Spectrometer (NIRI) and the Near-Infrared Integral Field Spectrograph (NIFS), and more recently with the Gemini Near-Infrared Spectrometer (GNIRS).

A major achievement in the Gemini AO program occurred during 2011 when the Gemini Multi-Conjugate Adaptive Optics System (GeMS) and its near-infrared imager, the Gemini South Adaptive Optics Imager (GSAOI), collected the first photons in the Chilean skies. GeMS is a unique facility instrument and the first of its kind.

Send e-mail to rcarrasco@gemini.edu

Adaptive Optics Systems III, edited by Brent L. Ellerbroek, Enrico Marchetti, Jean-Pierre Véran, Proc. of SPIE Vol. 8447, 84470N · © 2012 SPIE · CCC code: 0277-786/12/$18 · doi: 10.1117/12.926240

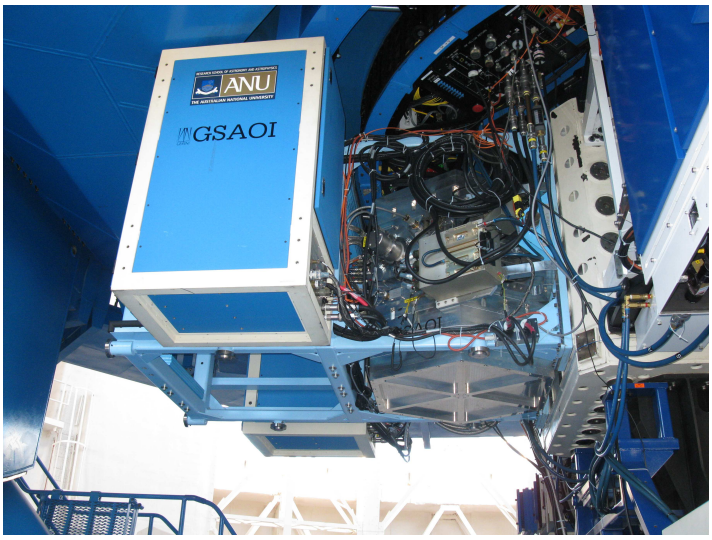

Figure 1. GSAOI after the installation on port 5 of the ISS. The Gemini South AO bench CANOPUS, is partially visible at the right corner of the picture.

Its delivers a uniform, diffraction limited image quality in the near-infrared (0.9 to 2.5 μm) over a field of view larger than 1 arcmin. The main GeMS sub-systems are the AO bench CANOPUS, the Beam Transfer Optics and Laser. Specifications for GeMS and its sub-systems are described in detail in previous papers.[1–4] Specifics of GeMS commissioning can be found in other presentations at this conference.[5,6]

GSAOI is a near-infrared adaptive optics imager and the workhorse instrument to be used with GeMS. It was built by the Research School of Astronomy and Astrophysics (RSAA) of the Australian National University. The GSAOI is located at the f/32 output focus of CANOPUS and can deliver diffraction limited images in the wavelength interval of 0.9 - 2.4 μm over a field of view of 85″×85″. The GSAOI detector is formed by four Rockwell HAWAII-2RG arrays, with 2040 × 2040 pixels each, with a pixel scale of 0.02″ on sky. The arrays are mounted in a 2×2 mosaic that create a 4080×4080 pixel focal plane with a gap of ∼2.5″ (∼2 mm) between arrays. The instrument is equipped with a set of broad- and narrow-band filters, a pupil imager to set the instrument alignment and defocus lenses to null the non-common-path phase errors between CANOPUS and GSAOI.

GSAOI has been delivered to Gemini South in 2007, after it passed the acceptance tests in 2006. The instrument has been extensively tested in the instrument laboratory located at the Gemini South base facility in La Serena, Chile, and then moved to Cerro Pachón in 2008. GSAOI remained in the instrument laboratory at the summit until January 13, 2011, when it was installed in one of the side looking ports (port 5) of the Instrument Support Structure (ISS) (Fig. 1). The GeMS commissioning started in January 2011 and extended until May 2011. The first two commissioning periods were dedicated to the laser and associated sub-systems. The commissioning of CANOPUS itself started only in March 2011. During the period of January 2011 - May 2011, we concentrated in the characterization of the GSAOI detector, the required calibrations to process the images (dark, flats) and imaging processing. The commissioning of GSAOI itself started in December 2011, when GSAOI was installed on port 1 (up-looking) of the ISS after a five month shutdown. In this paper we present and discuss our preliminary findings from the GSAOI commissioning, concentrating on detector characterization, on-sky performance and system throughput.

2. INSTRUMENT OVERVIEW

The GSAOI is at the back end of the GeMS science light path. The 2′ diameter f/32 GeMS output field is directed to GSAOI by the science fold mirror in the ISS. The beam passes through the GSAOI cryostat window (Fig. 2) and comes to focus 300 mm inside the cryostat field at a field mask. The central 85″×85″ science field

then passes through a double field lens and a four-element optical relay. The field lens forms a pupil image within the relay optics where the internal cold stop is located. Two filter wheels are located immediately in front of the cold stop. The optical relay re-images the input focal plane onto the image detector at a scale of $0.02''$/pixel. An utility wheel allows a lens group to be positioned temporarily between the relay and the detector to record the image of the cold stop. This cold stop image is used to accurately align the cryostat with the GeMS exit pupil. Convex and concave lenses, also in the utility wheel, produce defocused star images at the detector. These images are used to measure static wave front phase errors that are nulled using the GeMS deformable mirrors.[8] A detailed description of the instrument, including the imager optical design and detector characteristics, can be found in another paper.[7]

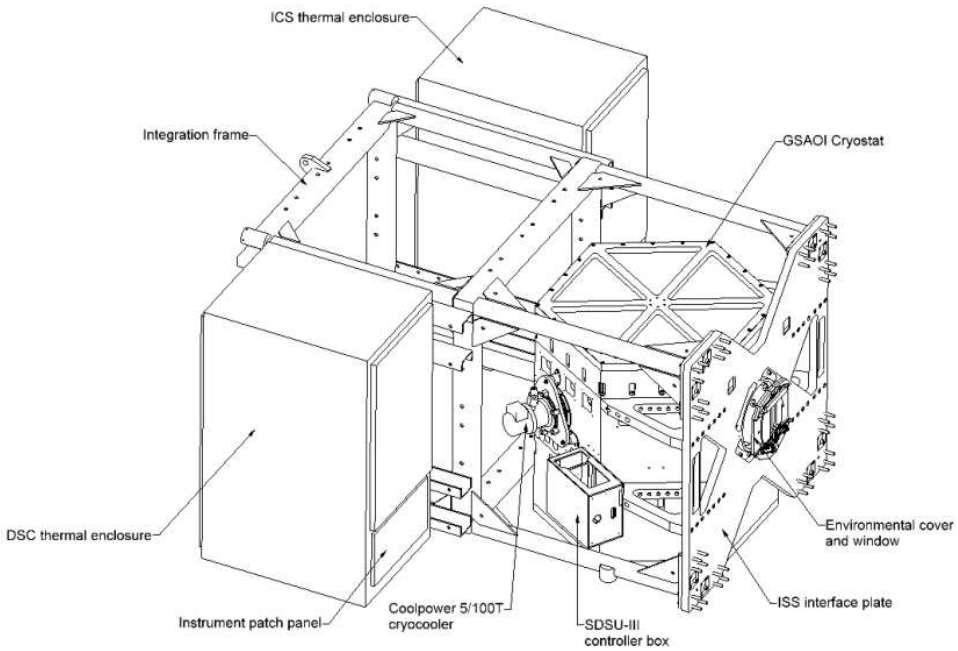

Figure 2. Schematic of the GSAOI cryostat and auxiliary systems.

2.1 Filters

GSAOI contains two filter wheels with space for 27 broad- and narrow-band (zero redshifted) emission- and absorption-line filters. Each filter wheel also contains one blocked position for recording bias and dark frames. Fig. 3 shows the transmission curves of the filters currently installed in GSAOI.

2.2 Detectors

The GSAOI science array is a 2×2 mosaic of Rockwell 2048×2048 HAWAII-2RG (H2RG) detectors forming a 4080×4080 pixel focal plane, with a gap of ∼2.5 mm or $\sim 2.4''$ on sky between each detector. Each detector is simultaneously read out through four 512×2048 pixel amplifiers for a shortest readout time of ∼5.3 seconds. The detectors have four additional rows and columns around the outer edges that read out as reference pixels and are not illuminated. Each detector also contains a programable On-Detector Guide Window (ODGW) which provides tip-tilt information to GeMS (see section 2.3).

The detectors are read out using the "Fowler Sampling" technique[9] to reduce the read noise. A set of multiple non-destructive reads is made at the beginning and at the end of each exposure. The two sets of non-destructive reads are averaged, and the signal is formed from the difference between the two averages. Each detector is continuously read out and reset in "idle" mode between science exposures. This prevents the detector saturating, and maintains the readout electronics at a stable operating temperature. When an actual exposure is initiated, the current idle

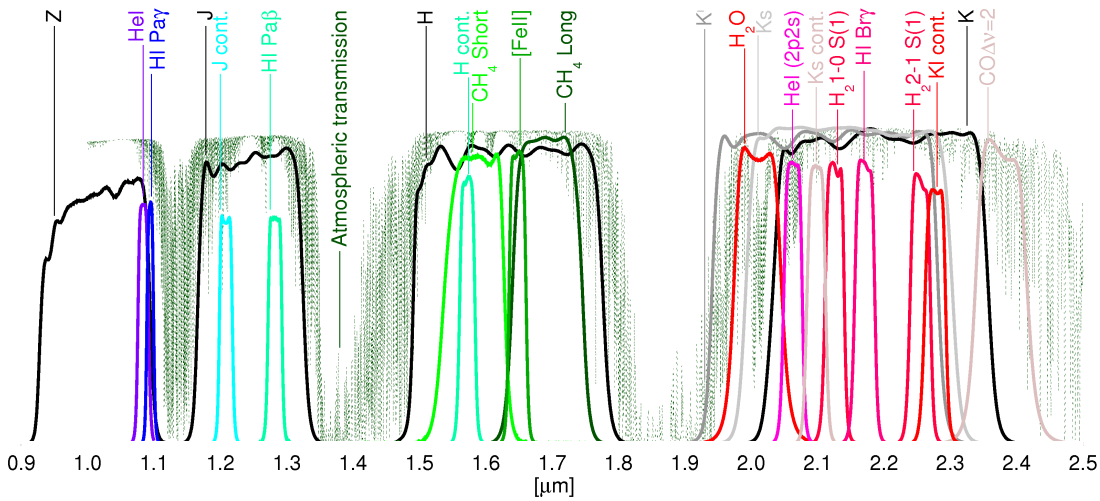

Figure 3. Transmission curves for the broad- and narrow-band filters installed in GSAOI. The atmospheric transmission between 0.9 and 2.5 μm is superimposed as a dark green line.

mode read is interrupted and the science exposure is started with the defined number of non-destructive reads. The definition and implementation of the three read-out modes in GSAOI for optimal observation of bright, faint and very faint objects are discussed in section 4.2.

The dark current in the GSAOI detectors is very low (∼0.01 e-/s/pix). However, there is a large number of "hot" pixels, which appear as a single high dark current pixel affecting to a lesser degree the four adjacent pixels, in a cross shape (Fig. 4, left panel). In addition, the cosmetics of the GSAOI detectors are affected by the presence of "dead" (debonded) pixels, light-emitting diodes, "cold" (lower response) regions, and higher dark current areas (Fig. 4, right panel). To correct and eliminate all these effects, a bad pixel mask is required for proper processing and analysis of the images.

The GSAOI detectors are intrinsically non-linear due to their source-follower-per-detector architecture. The linearity correction for each detector has been derived during commissioning and will be implemented as part of the GSAOI data reduction package (see section 4.1).

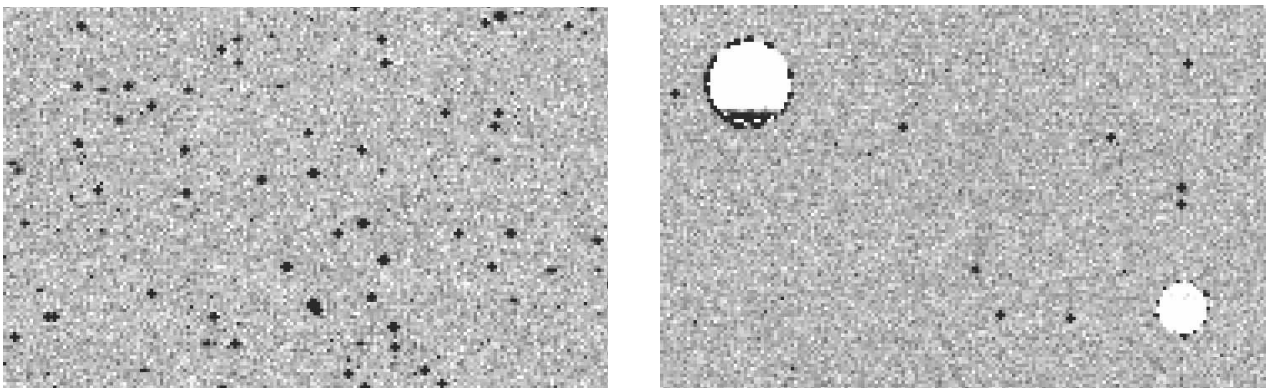

Figure 4. A 200 seconds GSAOI dark image observed in March 27, 2011. *Left:* region of the detector showing the cross-shaped "hot" pixels. *Right:* region of the detector showing cosmetic defects (dark and bright regions).

2.3 On-Detector Guide Window (ODGW)

Each of the GSAOI detectors can support one programmable ODGWs. The ODGWs are designed to provide tip-tilt information for a combination of up to four natural guide stars in GeMS. The ODWGs can be read out at a rate of up to 800 Hz during a science exposure. Sizes of 2×2, 4×4, 6×6, 8×8, 12×12, 16×16, 32×32, 64×64 or 128×128 pixels can be specified, although it is expected that most science observations will be carried out using 4×4, 6×6 or 8×8 pixel windows in order to achieve higher correction rates. The centroid of the stars located in the ODGWs are used for either CANOPUS tip-tilt correction or for fast guiding to correct for the differential flexure between GeMS and GSAOI. Each of the four ODGWs can be read out with a different rate, as long as each exposure time is an integer multiple of the shortest exposure time selected. The four ODGWs are read out synchronously using non-destructive reads, interleaved with the reads of the science image during resets and Fowler Sampling. This requires a reduction of the ODGWs frame rate to ∼200 Hz during the periods when the science image is being accessed. Otherwise, the science image read out time would be unacceptably long.

The use of the ODGWs for CANOPUS tip-tilt correction has not been commissioned at this point. It is expected that we will be commissioning this mode (1+3, one CANOPUS Tip-tilt Guide Star + three ODGWs) during the second semester of 2012 (see section 6). Further specification about the use of the ODGWs with GSAOI, with corresponding detector controller software implementation and performance required by GeMS can be found in another presentation at this conference.[10]

3. COMMISSIONING STATUS

The GSAOI commissioning was divided in two phases. The first phase took place between January and May 2011. During this period, the commissioning work concentrated in the definition of the GeMS non-common-path aberration[5,8] and the characterization of the GSAOI detectors, with the determination of the read noise, gain, and linearity. The phase one commissioning results are presented in section 4.

The second phase of the GSAOI commissioning took place between December 2011 and April 2012. During this phase, the work was focused on the GSAOI on-sky performance: accurate determination of the instrument alignment angle and astrometric solution for each detector, photometric zero points, and sky brightness measurements in J-, H- and K_s filters, estimation of the background contribution from GSAOI and CANOPUS, and measurement of the system throughput. Although the bulk of the work between January and May 2011 was concentrated on GeMS, some data were obtained to evaluate the GSAOI on-sky performance in May 2011. The on-sky commissioning results are presented in section 5.

4. COMMISSIONING RESULTS: DETECTOR CHARACTERIZATION

4.1 Linearity correction

As with all near-IR arrays, the GSAOI detectors are intrinsically non-linear. To obtain the linearity correction, a set of flats of increasing exposure time were observed using the Gemini Calibration Unit (GCAL[11]) in the H- and Z-bands. The data were taken using a Fowler Sampling of 1-1 (NRDs=2).

The linearity correction was implemented using a polynomial fit to the raw data counts (ADU):

$$\text{linearity correction factor} = a + b \cdot ADU + c \cdot ADU^2 \tag{1}$$

To obtain the coefficients a, b and c, a second order polynomial with uniform weighting was fit to data points corresponding to the average count values on twelve regions for each detector, three on each amplifier. Table 1 shows the resulting linearity correction for each of the four detectors using the H-band and Z-band data. As an example, the left plot in Fig. 5 shows the linearity correction derived for detector 4.

The results presented in Table 1 were obtained from data with count levels above 3000 ADU. Additional data were obtained to analyze the linearity behavior at low light levels, i.e. below 3000 ADU. The analysis indicates the presence of a non-linear behavior of increasing response towards lower levels of illumination (in other words, in the opposite sense of the above fitted function). However, the scatter in the data points, due to the low level of

Table 1. Final linearity correction parameters.

Detector	a	σ_a	b	σ_b $[\times 10^{-7}]$	c $[\times 10^{-7}]$	σ_c $[\times 10^{-11}]$	Correlation	σ_{res}
1	0.9947	0.0007	7.4	0.7	2.5	0.1	0.993	0.003
2	0.9940	0.0010	6.0	1.0	3.7	0.3	0.989	0.005
3	0.9947	0.0006	7.1	0.6	2.2	0.1	0.991	0.003
4	0.9959	0.0006	5.7	0.6	2.7	0.1	0.991	0.003

counts and presence of bad pixels, is as large as the effect that we are trying to measure. We concluded that non-linearity effects at low levels may affect the photometry of faint sources, with sources at or below 300 ADU total counts, including sky background contribution, resulting 2-4% brighter than they should be relative to sources at ∼2000 ADU. However, a 2-4% uncertainty is what we expect to achieve in the photometric calibration (see section 5.2). Given the uncertainties in the data at low luminosity levels, only the linearity correction presented in Table 1 is implemented in the data reduction package.

After the linearity correction was obtained, the data were examined to determine the saturation value and the count levels (in percent of the saturation level) where the data diverges 5% from linear (before linearity correction). These values are listed in Table 2. The table also shows the level where the linearity corrected values diverges 2% from the linear relation.

Table 2. Final linearity correction parameters.

Detector	Saturation [ADU]	5% (without correction)	2% (with correction)
1	52400	73%	97%
2	50250	64%	97%
3	53700	76%	98%
4	52300	75%	96%

The implementation of the linearity correction has been done in the GSAOI IRAF package (under development), as part of the task GAPREPARE. The right plot in Fig. 5 shows an example of the data described in this section before and after correction for detector 4, using the final linearity correction values listed in Table 1. The dashed lines in the figure indicate the saturation level before and after linearity correction.

4.2 Readout noise and gain determination

The read noise for each detector was determined using dark exposures for four different Fowler Sampling modes: 1-1, 4-4, 8-8 and 16-16. These modes correspond to NDRs of 2, 8, 16 and 32 respectively. We have used the Fowler-Mortara Mean-Variance analysis method to calculate the read noise and the gain.[12] In summary, the variance in ADU of an image can be represented as

$$V_{ADU} = (RN_{ADU})^2 + S_{ADU}/g \tag{2}$$

where V_{ADU}, RN_{ADU} and S_{ADU} are the variance, the read noise and the signal in ADU and g is the conversion gain in e-/ADU. By plotting the variance as a function of the mean signal, one should get a straight line whose Y intercept is $(RN_{ADU})^2$ and slope is $1/g$.

The dark images for each read mode were combined, and the variance image was obtained as the standard deviation of the input pixel values about the output combined pixel value. The pixel statistic was then obtained by taking the mean of each array using a two-pass statistics with 1-sigma rejection (due to the large number of

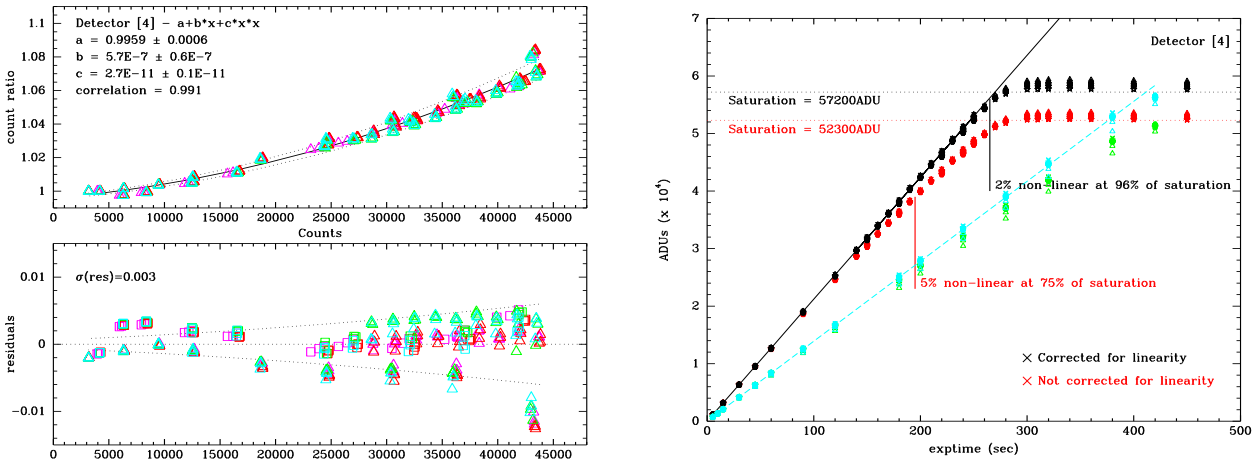

Figure 5. *Left:* Resulting linearity correction for detector 4 using the H-band and Z-band data, fitting the full set of points (all amplifiers). *Top panel:* linearity (count ratio) as a function of total counts. Each color corresponds to one of the amplifiers (1 = pink, 2 = red, 3 = green, 4 = blue; amplifiers are numbered left to right in each array). The dashed lines indicate the 1-sigma envelope of the fitted function. The H-band data are represented by triangles, the Z-band data by squares. *Bottom panel:* residuals (fit - data) as a function of total counts. *Right:* Linearity corrected H and Z data for detector 4, using the parameters from Table 1. The red and green points are the uncorrected H and Z data respectively; the black and blue points correspond to the H and Z data, respectively, after the correction has been applied. The black/blue slanted lines correspond to the loci of a constant ADU rate. The dashed horizontal lines correspond to the saturation level before and after the linearity correction. The 5% and 2% non-linearity levels are also indicated, respectively before and after the correction has been applied.

bad pixels in the GSAOI detectors). The median value obtained after the second pass corresponds to the final $(RN_{ADU})^2$.

The e- to ADU gain for each detector was determined using the same dataset used for the non-linearity determination, for count levels up to 35000. The flat images for each exposure time were combined and the variance image was calculated as for the darks. To calculate the gain values, equation 2 was slightly modified, and the following expression was used:

$$\log[V_{ADU} - (RN_{ADU})^2] = \log(S_{ADU}) - \log(g) \tag{3}$$

The advantage of plotting the read-noise subtracted variance against the mean signal on a logarithmic scale is the removal of one degree of freedom in the fit, as the read noise is already known, and the fit is now a straight line of slope 1.0, with the X intercept being the gain g.

Table 3. Detector gain and readout noise values as a function of Fowler Sampling.

	Read noise [ADU]				Gain
Detector	$FS1-1$	FS 4-4	FS 8-8	$FS16-16$	[e-/ADU]
1	11.6	5.6	4.2	3.2	2.434
2	9.5	4.9	3.7	2.9	2.010
3	11.2	5.9	4.4	3.3	2.411
4	12.4	6.3	4.8	3.7	2.664

The calculated readout noise and gain for each detector are listed in Table 3. As we can see in the table, the average readout noise for a $NDR = 2$ (FS 1-1) is ∼11 ADU. It can be reduced to ∼3 ADU using a 16-16 Fowler

Sampling ($NDRs = 32$), but this decrease in noise is penalized by an increase in the readout time from ∼10 to ∼90 seconds. Using a 8-8 Fowler Sampling, the readout noise is only ∼1 ADU higher than the 16-16 mode, but the readout time is much shorter (∼48 seconds). Table 4 summarizes the three read-out modes implemented in GSAOI for observations of bright, faint and very faint objects. The table includes information about the readout time and the minimum exposure required for each mode.

Table 4. Readout modes implemented in GSAOI.

Mode	Fowler Sampling	NDRs	Read Noise	Readout time	Min. Exp. Time
Bright Object	1	2	28 e-	10.0 sec	5.3 sec
Faint Object	4	8	13 e-	26.2 sec	21.1 sec
Very Faint Object	8	16	10 e-	47.7 sec	42.2 sec

4.3 Dark current and dark stability

We have analyzed the dark current behavior in the GSAOI detectors, concentrating on its impact on operational procedures and data reduction. A set of dark images with exposure times between 5.3 seconds and 200 seconds were taken to identify for any dark current spatial structure and spatial variations. The same sequence of darks was repeated for three consecutive days, spaced by ∼20 hours, to explore variations in time scales of a few minutes to several hours, i.e., within an observation and from one night to another. From the above analysis, we conclude the following:

- The dark current shows spatial structure within each detector. The level of the structures can be up to ∼10 ADU above the mean dark current level of the entire detector, but it is of the order or smaller than the standard deviation of the pixel values around that mean. Consequently, in any dark subtracted image, the residual dark structure will be within the noise.
- The dark current is found to be variable on time scale of minutes to hours within each detector. The amplitude of the variations on time scales of minutes (within an observation) is of the order of 2-6 ADU, and smaller than standard deviation around the mean values, so again in any dark subtracted image, the variations in the dark current will be lost in the noise.
- From a data reduction point of view, dark subtraction in the form of dark frames of the same exposure time as the science data is not required, as long as the dark current is subtracted as part of the data reduction process itself, as normally happens in standard near-IR observations using dithered sequences for sky subtraction.

5. COMMISSIONING RESULTS: ON-SKY PERFORMANCE

Analysis of the GSAOI on-sky performance is based on data collected in May 2011, and between December 2011 and April 2012. Before we proceed with the analysis of the data, it is important to mention that four major events affected the photometric results, changing the values of the sky brightness, photometric zero points, and system throughput. The first event occurred after the GSAOI installation in January 2011. The commissioning team discovered that the flatfield images showed an illumination in the central region of the field of view. This "ramp up" effect was stronger in the K-band. Further analysis of the data showed that the GSAOI cryostat window was contaminated by dust on its external surface, affecting the performance of the instrument, in particular at wavelengths greater than 2 μm. The second event happened in November 2011, when the cryostat window was cleaned and the dust was removed, prior to the instrument re-installation. The third even took place in February 2012, when the cryostat window was found to have suffered damage to the AR coating, which compromised the quality of the data obtained during this commissioning run. The last event occurred in March 2012, when the damaged cryostat window was replaced by a new one. GSAOI was removed from the telescope in March 2012 due to a problem with the cryo-cooling system. The instrument returned to the telescope for the last two

commissioning runs in April 2012 when data were obtained to characterize the instrument with the new cryostat window.

5.1 Data set

The images collected during on-sky commissioning were used to determine and monitor the photometric zero point and sky brightness, and to calculate the end-to-end system throughput. In addition, sky frames were observed to determine the background contributions from individual sub-systems, in particular, from CANOPUS. A summary of the observed data is presented next. The observing log is presented in Table 5.

- *May 2011:* The observations consist in several exposures in the J, H and and K_s filters of a region adjacent to the Galactic globular cluster NGC 6352, and a nearby sky region. Twilight flats were obtained during the same period to serve as flat field frames. This is the first data set obtained to quantify the GeMS+GSAOI on-sky performance. The image quality was not optimal, as the GeMS performance was still being optimized, with an average Full Width Half Maximum (FWHM) of ∼32 pixels (∼0.64″) in H-band.
- *December 2011:* The data used for the analysis consist of a stack of thirteen exposures of 60 sec, observed with 3″ offsets between individual frames, of the Galactic globular cluster NGC 288. The average FWHM of the combined image is slightly below 0.08″, with a variation of 0.002″ across the entire field of view. This is the "first light" ultra-sharp, wide field image observed with GeMS+GSAOI.[8,13]
- *January 2012:* The data set consists of several exposures in the J, H and K_s filters of a 2MASS (the Two Micron All Sky Survey) standard calibration field.[14] The image quality was not optimal, with an average FWHM of ∼28 pixels (∼0.56″).
- *February 2012:* The data obtained during this run consist of several exposures in the J, H and K_s filters of an astrometric calibration field located in the Large Magellanic Cloud (LCM). The average FWHM in the H-band combined image is ∼ 9 pixels (∼ 0.18″).
- *April 2012:* The data used for the photometric calibration consist of several exposure in J, H and K_s filters of a 2MASS standard calibration field.[14] The FWHM in the H and K_s filters is on average ∼7 pixels (∼0.14″). Also, sky frames were observed in all filters to determine the background contribution of the different sub-systems.

Table 5. Observing log

Observing Date (UT)	Object	Filter	Exposure time (sec)	FWHM (pixels)
2011 May 18	NGC 6352	J	1×20	32.0
		H	4×20	
		K_s	4×45	
2011 Dec 16	NGC 288	H	13×60	4.0
2012 Jan 12	2MASS Calibration Field	J, H, K_s	5×60	28.0
2012 Feb 15	LMC	J	1×15	9.0
		H	4×90	
		K_s	1×15	
2012 Apr 07	Blank Field	All filters	1×300	
2012 Apr 12	Blank Field	All filters	1×180	
2012 Apr 15	2MASS Field	J, H, K_s	9×15	7.0
2012 Apr 30	2MASS Field	H	4×45	11.0
		K_s	4×60	7.0

All images were processed using the GSAOI IRAF commissioning package developed by the commissioning team. The images were corrected for non-linearity using the task GAPREPARE, then for each filter, a set of flats were processed, combined and normalized using the task GAFLAT. Sky frames were constructed using the task GASKY. The science images were then processed using GAREDUCE. The latter task handles the sky subtraction, flat-fielding and multiplication by the gains. The resulting images were then mosaiced with GAMOSAIC. For the fields with observations obtained with spatial offsets between the exposures, the images were registered to a common pixel position and then stacked.

5.2 Photometric zero point and sky brightness

The photometric zero points in the J, H and K_s filters were measured using aperture photometry with the DAOPHOT package in IRAF. For each star, the aperture photometry was obtained using an aperture typically 1.4× the FWHM. For the sky background estimation, an inner-sky annulus and outer-sky annulus were selected based on the FWHM values of the stars and the final aperture correction was applied to the data. Typically, the values selected were between 40 and 103 pixels for the inner-sky annulus, with a width of 11 pixels in all cases. For the May 2011 data, the photometry was performed with the task IMEXAMINE, using an aperture radius of 40 pixels, a buffer of 10 pixels, and a background annulus of 40 pixels.

The instrumental magnitudes in the CANOPUS+GSAOI system were calculated as follows:

$$m_\lambda = -2.5 \cdot \log(F_\lambda) \tag{4}$$

where m_λ is the instrumental magnitude, F_λ is the flux in e-/s and λ is the wavelength corresponding to filters J, H and K_s.

The resulting values for the instrumental magnitudes were then compared with the 2MASS standard magnitudes to define the zero points. Excluding the May 2011 data, an airmass correction was introduced using the values for the atmospheric extinction calculated for the 2MASS catalog ($A_J/A_H/A_{K_s} = 0.092/0.031/0.065$).[14] The photometric zero points obtained for the different observing runs are shown in Table 6. The sky brightness values, converted from the average counts in the sky frames, are tabulated in Table 7.

Table 6. Photometric zero-points values

UT Date	Filters			Comments
	(j-J^{2MASS}) [mag]	(h-H^{2MASS}) [mag]	(k_s-K_s^{2MASS}) [mag]	
2011 May 18	-26.59	-26.63	-26.17	Dust in the cryostat window
2011 Dec 16		-26.75		Cryostat window cleaned
2012 Jan 12	-26.30	-26.51	-25.95	
2012 Feb 15	-26.09	-26.01	-25.08	Coating problem in the cryostat window
2012 Apr 15	-26.43	-26.72	-26.12	New cryostat window installed
2012 Apr 30		-26.65		

The photometric zero-points values from the different runs are found to be reasonably stable, except for February 2011, when the coating in the central region of the GSAOI cryostat window was damaged. The same behavior is seen for the sky brightness. The higher sky signal derived in May 2011, compared to the values from December 2011, is due to the dust contamination on the cryostat window. Note how the effect of coating damage on the window is evident in the sky brightness measured in February 2012. Comparing the results in Table 7 with the published values for Cerro Pachón available from the Gemini Web pages (the estimated values for Cerro Pachón are $\mu_J = 16.2$ mag/arcsec^2, $\mu_H = 13.8$ mag/arcsec^2 and $\mu_K = 14.6$ mag/arcsec^2) we found that, at 1.65 μm (H-band) the calculated sky brightness for April 2012 is similar to the value estimated for Cerro Pachón, but we also see large differences, up to a factor of 2 in the surface brightness at 1.2 μm (J-band) and 2.2 μm (K-band). The latter may be due to an underestimation in the thermal contribution from CANOPUS. We analyze this effect in more detail in section 5.4.

Table 7. Sky brightness values

Filters	J		H		K_s	
UT Date	Flux [e-/s/pix]	μ_J [mag/arcsec^2]	Flux [e-/s/pix]	μ_H [mag/arcsec^2]	Flux [e-/s/pix]	μ_{K_s} [mag/arcsec^2]
2011 May 18	18.28	14.94	94.80	13.19	169.92	12.10
2011 Dec 16			96.87	13.29		
2012 Jan 12	7.27	15.65	54.32	13.68	129.38	12.18
2012 Feb 15	10.07	15.09	54.00	13.18	158.13	11.09
2012 Apr 15	11.26	15.31	58.85	13.80	125.78	12.38
2012 Apr 30			48.97	13.93	111.35	12.52

5.3 System Throughput

In this section, we calculate the end-to-end system throughput from the zero-points measured above. The stellar flux above the Earth's atmosphere is given by the standard equation using the absolute flux calibration of the photometric system. For the analysis, the following values were adopted:

$$I_J = 1520 \times 10^{-0.4J}[Jy] \tag{5}$$
$$I_H = 980 \times 10^{-0.4H}[Jy] \tag{6}$$
$$I_K = 650 \times 10^{-0.4K}[Jy] \tag{7}$$

The detected stellar flux is then:

$$F_\lambda = \frac{10^{-19}\ I_\lambda(Jy)\ A_{tel}(m^2)\ \tau_\lambda}{h\nu}\ [e\text{-}/s/Hz] \tag{8}$$

or

$$F_\lambda = 1.509 \times 10^{-7}\ I_\lambda(Jy)\ A_{tel}(m^2)\ \tau_\lambda\ \frac{\Delta(\lambda)}{\lambda}\ [e\text{-}/s] \tag{9}$$

where $A_{tel} = 48.23$ m^2 is the telescope area. Replacing equations (5-7) in equation (9), we have

$$F_J = 1.770 \times 10^{11}\ 10^{-0.4J}\ \tau_J\ (e\text{-}/s) \tag{10}$$
$$F_H = 1.297 \times 10^{11}\ 10^{-0.4H}\ \tau_H\ (e\text{-}/s) \tag{11}$$
$$F_K = 8.601 \times 10^{10}\ 10^{-0.4K}\ \tau_K\ (e\text{-}/s) \tag{12}$$

after some further manipulation, the system throughput τ_λ can be expressed as follow:

$$\tau_J = 10^{-11.25+0.4\ (j-J)} \tag{13}$$
$$\tau_H = 10^{-11.11+0.4\ (h-H)} \tag{14}$$
$$\tau_K = 10^{-10.94+0.4\ (k-K)} \tag{15}$$

where $(j - J)$, $(h - H)$ and $(k - K)$ are the zero points listed in Table 6. The system throughput values are listed in Table 8 (the results from February 2012 are not included in the table, as the partially uncoated window turns those values unreliable).

Table 8. System throughput values

Run	τ_J	τ_H	τ_{K_s}
May 2011	0.24	0.35	0.34
Dec 2011		0.39	
Jan 2012	0.19	0.32	0.28
April 2012	0.21	0.38	0.32

For H and K-band, the system throughput obtained in April 2012 is better than the throughput assumed for the instrument initially,[15] while for J-band it is similar (the assumed sensitivity is 0.23 at all wavelengths, McGregor). However, it is possible that the improvement in the sensitivity could be offset by the sky signal which is brighter than expected at wavelength larger than 2 μm (see section 5.4).

5.4 Background brightness

The expected image sensitivities for GSAOI are based on theoretical models for the combined telescope, instrument and GeMS transmission and emissivity and assumes a set of values for the background contribution from each of these sub-systems. The atmospheric airglow is expected to be the main contributor to the background signal at short wavelengths. The second contributor is thermal emission from CANOPUS.[15] Before a photon arrives to GSAOI, it has to pass through several optical elements that can increase the background signal, in particular at wavelengths larger than 2 μm.

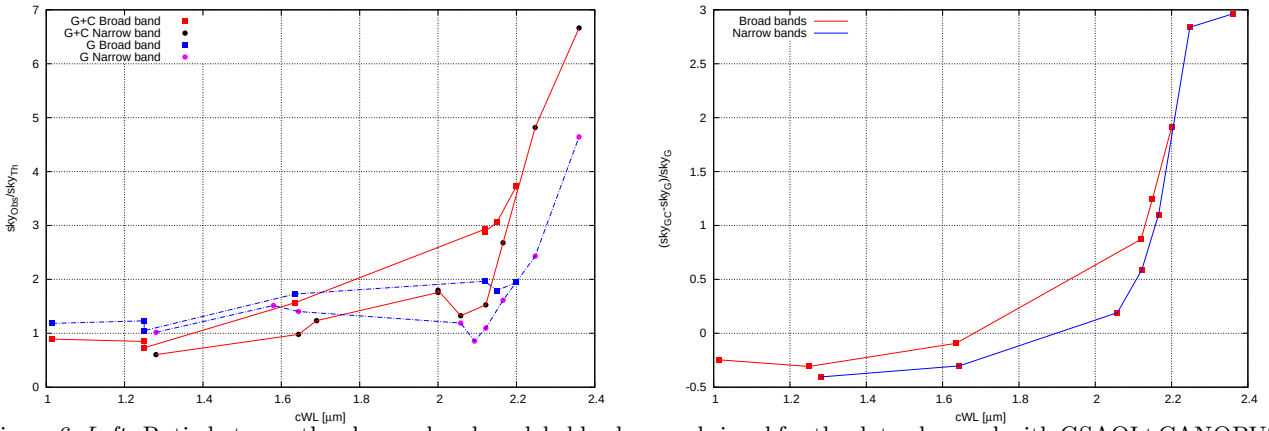

Figure 6. *Left:* Ratio between the observed and modeled background signal for the data observed with GSAOI+CANOPUS (orange squares and blue dots) and data observed with GSAOI only (blue squares and red dots). *Right:* Difference in the background signal between the data obtained with the configuration GSAOI+CANOPUS and with GSAOI only, relative to the background obtained with GSAOI only.

To determine the background signal in each filter, and in particular, the background contribution from CANOPUS, a blank, star-free area of the sky was observed in 17 filters in April 2012 (see Table 5). Two datasets were obtained. The first set of data were taken using GSAOI+CANOPUS, while the second set of data were obtained with GSAOI looking directly to the secondary mirror, by-passing the entire CANOPUS optics*. Both dataset were dark subtracted, although it was found that the dark current does not affect the results, as expected. A region in each detector was selected in a way to avoid the few sources detected, as well as areas with large concentration of bad pixels, and the mean and standard deviation of the counts in each filter was obtained to calculate the average sky flux, which was then corrected by the transmission value of the filter.

The left plot in the Fig. 6 shows the ratio between the observed and the modeled background contribution (available in the GSAOI web page, see[15]). The first thing to be remarked in this plot is that the original

*In April 2012, GSAOI was installed on the up-looking port of the ISS (port 1)

model underestimates the background contribution from GSAOI+CANOPUS for wavelengths greater than $\sim$ 1.6 μm (orange squares and black dots). When compared to the data observed with GSAOI only, the model underestimates the background contribution for wavelengths greater $\sim$2 μm (blue squares and red circles). The right plot in the Fig. 6 shows the ratio of the difference in the background signal between the data obtained with GSAOI+CANOPUS and with GSAOI only, to the background obtained with GSAOI only. This plot isolates the CANOPUS background contribution, and shows that, for wavelengths below $\sim$1.6 μm, CANOPUS attenuates the science path light about 30%, while for wavelengths larger than $\sim$1.6 μm, CANOPUS is emitting at a factor or 2 or more than the contribution from the instrument alone.

Figure 7 shows the difference in the background signal between the data obtained with the configuration GSAOI+CANOPUS and with GSAOI only, calibrated in flux. The color lines represent the thermal emission expected from a black body with temperatures between $-10\,^{\circ}C$ and $+10\,^{\circ}C$, in steps of $5\,^{\circ}C$, corrected for the absorption introduced by the optics inside CANOPUS. We can see here that the CANOPUS contribution to the background can be approximated by a black body with temperature $0 - 5\,^{\circ}C$, which is compatible with the temperature measured by the sensors located inside the CANOPUS enclosure.

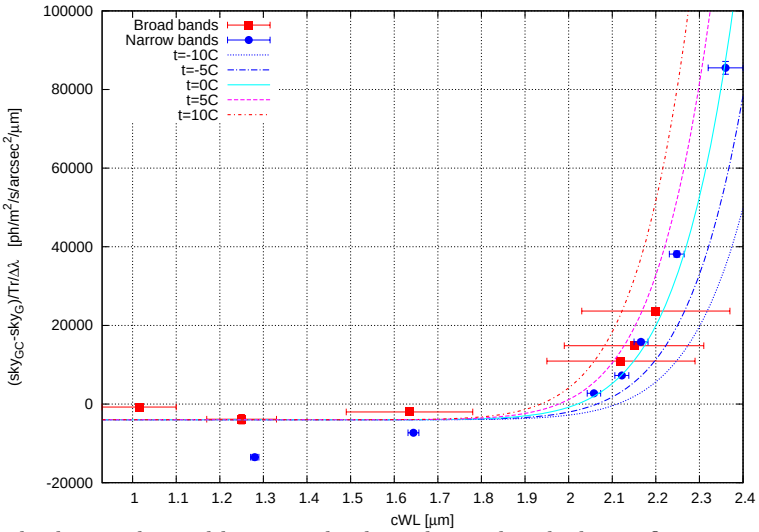

Figure 7. Difference in the background signal between the data obtained with the configuration GSAOI+CANOPUS and with GSAOI only in units of ph/s/arcsec^2/μm/m^2. The lines represent the thermal emission from a black body (see the text).

5.5 World Coordinate System calibration

The science data generated by any Gemini instrument must be calibrated to allow conversion between the x, y position to right ascension and declination. The conversion is dependent on the specifics of the instrument and the telescope configuration at the time of the data acquisition. The WCS solution in the header of the images is constructed based on information provided by the telescope systems: the equinox, the azimuth and elevation, the observing wavelength, the catalog (FK4 and FK5) at the time of the observation and port where the instrument is installed; and by the instrument: binning, detector size, WCS calibration file. The accuracy of the WCS solution in the images is directly linked to how accurately the WCS calibration file is constructed. And the accuracy of the WCS calibration file depends on the accuracy of the astrometric catalog used to derived the solution.

GSAOI is a mosaic of four detectors. Therefore, for each detector a WCS calibration file has to be constructed using a common reference point. GSAOI was installed on port 5 between January and May 2011 and moved to the up-looking port in December 2011. The orientation of the instrument on the sky is different when it is installed on different ports. The GSAOI orientation on port 5, for an instrument alignment (IAA) and position angle (PA) = 0 degrees, is N-left and E-down. In the up-looking port, for the same IAA and PA, the GSAOI orientation is N-up, E-right.

In May 2011 a single observation of the Galactic globular cluster NGC 6352 was used to derive the WCS solution for the GSAOI detectors on port 5. The UCAC3 catalog[16] was used to select the stars in the field. The positional accuracy of stars in UCAC3 is about 15-20 milliarcseconds for stars in the 10 to 14 magnitude range in R. Unfortunately, stars brighter than 14 mag in R were saturated in the GSAOI images and only a reduced number of stars were used. The WCS calibration files were derived using the IRAF task GWCS. The procedure is the following:

- The reference point is defined to be at the telescope rotator axis. The location of the reference point is not coincident with the center of GSAOI detector. The reference position in pixels was measured in advance (it is located in the gap between the detector 3 and 4).
- The right ascension (RA) and declination (DEC) offsets from the reference stars to each other star in the input catalog are computed and translated into arcsec. Then the calculated RA, DEC offsets are translated into the telescope X and Y offsets using the PA and the IAA. In this case the $PA = 0.0$ deg. and the $IAA = 89.62$ deg (orientation N-up, E-left).
- All offsets are translated to millimeters using the telescope plate scale from the Telescope Control System.
- The output files, one per detector, contain 4 columns: the measured position of the stars in pixels coordinates x,y and the corresponding offset of the stars at the focal plane in millimeters.
- The WCS calibration files are incorporated into the detector controller software.

The final positional accuracy of the WCS calibration is $\sim 1''$ ($\sim$50 pixels). This accuracy is expected because the CANOPUS corrections were not optimal, with an average FHWM of the stars of $\sim$43 pixels.

In January 2012 a single image of an astrometric field located in the Large Magellanic Cloud was used to construct the WCS calibration files for the detectors with GSAOI installed in the up-looking. A catalog with a positional accuracy of 1 milliarcseconds[17] was used to select the stars in the field. The WCS calibration files were derived using the procedure described above. The accuracy of these WCS calibration files has been estimated to be $\sim 0.3''$ ($\sim$15 pixels) on average. This value is better than the results obtained in May 2011, but still not optimal. The average FWHM of the stars in the field is $\sim$ 9 pixels. Therefore, we expect to improve the accuracy in future measurements.

6. GSAOI AND THE GEMINI OBSERVING TOOL

The Gemini Observing Tool (OT) is the software used to define the instrument configuration and pre-plan the observations from approved proposal during the Phase II process. The OT is the principal interface between the astronomer and the observatory, and it is used by the night time observer to trigger an observation during a night.

The commissioning of any new instrument at Gemini has to include the necessary tests to validate the OT. As part of GSAOI commissioning, the OT has been extensively tested since the first commissioning run in January 2011. Here we described the main capabilities of the OT, focusing on the description of the GSAOI and GeMS components, guide star selection and observing preparation. Basic information on the OT itself is available elsewhere.[18,19]

The principal configuration components in the GSAOI observation (Fig. 8, upper panel) are the GSAOI component (Fig. 8, lower left panel) and the GeMs component (Fig. 8, lower right panel). The user can configure the GSAOI component by selecting the desired filter, the position angle, the readout mode (see section 4.2), the ISS port, the exposure time and number of coadds per image. The GeMS component editor is always included in any GSAOI observation. By default, the Atmospheric Dispersion Corrector is off, the Dichroic Beamsplitter is set to 1 μm and the Astrometric mode is regular.

The NGS can be sensed using either the CANOPUS tip-tilt guide stars (TTGS or CWFS), or the GSAOI ODGW, or any possible combination of the above. Ideally, three of these guide stars should be available to compensate for

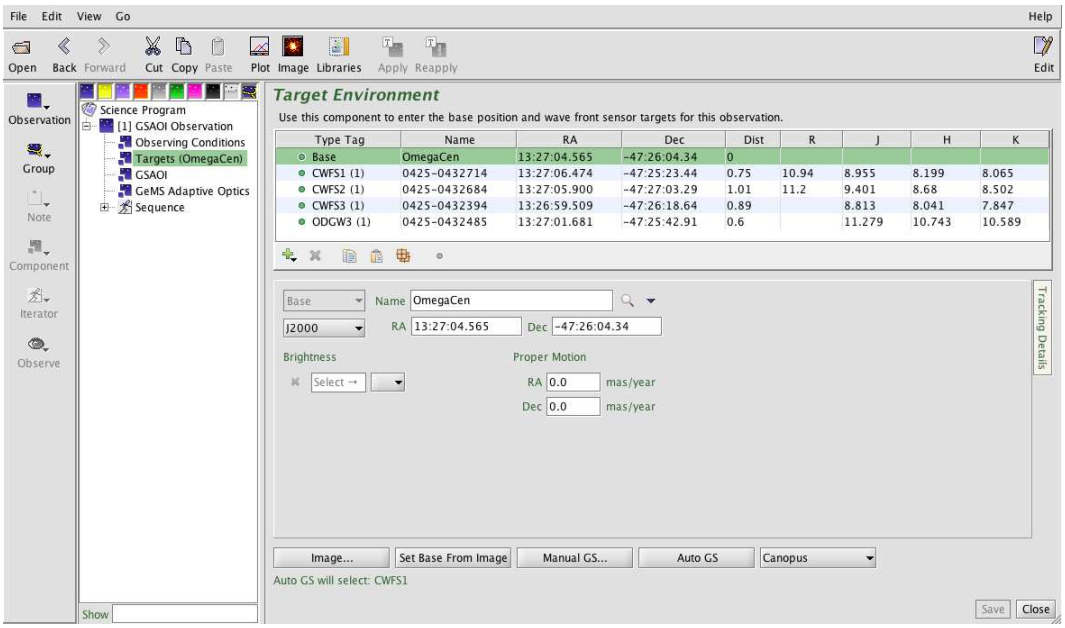

Figure 8. *Upper panel:* GSAOI observation defined in the OT. *Lower left panel:* The GSAOI component editor. *Lower right panel:* GeMS component editor.

the plate-dynamical errors. However, CANOPUS may work with 2 or even 1 CWFS with reduced performance. One of the ODGW stars is used to monitor and compensate the flexure drift between CANOPUS and GSAOI.

The CWFS and ODGW stars are specified in the target section of the main GSAOI observation (see upper panel in Fig. 8). The OT can select automatically the guide stars for all instruments and WFS using the "Auto GS" button in the target component or in the position editor (PE, see below). Alternatively, the selection can be done manually, using the "Manual GS" button in the target component (or in the PE).

The selection of CWFS and ODGW stars is performed using MASCOT (Multi-Conjugate Adaptive Optics Tool) algorithm developed by Francois Rigaut.[20] The algorithm searches different catalogs for TTGS at given coordinates, compute the best TTGS groups that will provide the best compensation (best Strhel) across the $2'$ CANOPUS field of view. The best asterism, based on the best average Strhel, is then selected by default. In manual mode, the GeMS guide star search window is displayed. In this window the user can configure the catalog, the NIR band, the asterism (CANOPUS and GSAOI, CANOPUS alone or GSAOI alone) and if a position angle adjustment is required or not. The GeMS guide star window search is shown in Fig. 9. When a query is requested, a list of guide star candidates inside the CANOPUS field of view (left panel in the figure) is given. This list can be reviewed and modified if needed. Then the algorithm performs an search for the best

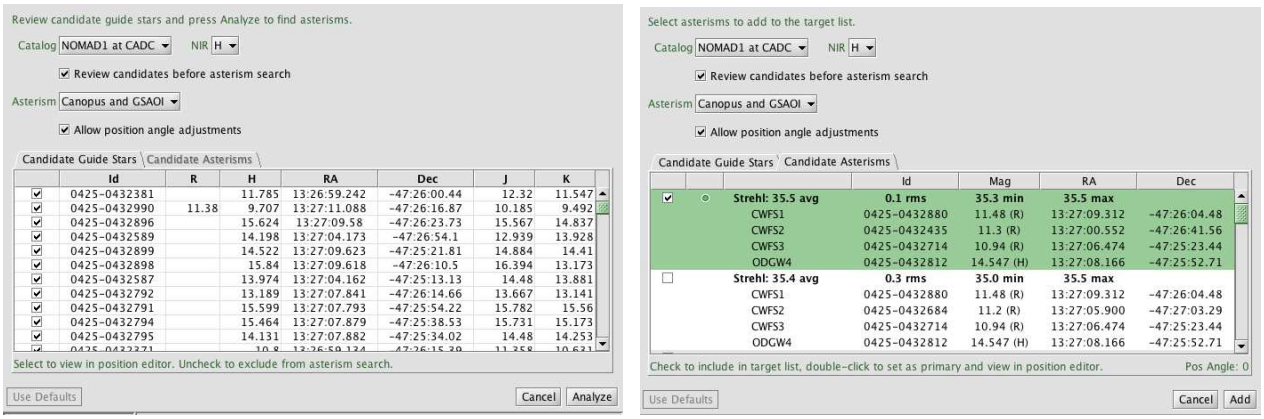

Figure 9. GeMS guide star search window. The left panel shows the list of potential stars used by MASCOT to search for the best asterism. The right panel shows the result of the search. The best asterism is highlighted in green. The user has the option to select one or more asterisms from the candidate list and add them to the target component.

asterisms and returns a list of candidates sorted by the average Strehl and the average *rms* (right panel in the figure). The algorithm can handle also sub-optimal cases. For example, it can return the best two-star asterism if a three-star asterism is not available. The user can also select more than one candidate asterism. When two or more asterisms are included in the target component, they are grouped separately.

The selected asterism can be viewed in the PE (Fig. 10). The GSAOI detector arrays are the large squares and identified with a number (the orientation is N-up, E-left). The GSAOI base position, defined in the target component, is marked as a small cross within a circle. It is located at the bottom right corner of detector 4, $\sim$7.6″ from the center of the CANOPUS field. The CANOPUS field of view is represented by a large circle with a radius of 1′.

During the commissioning runs only one guide mode has been tested. The majority of the engineerinwerg observations were obtained using 3 CANOPUS CWFS and 1 ODGW stars. Some observations were obtained with 2 CWFS and 1 ODGW stars, or with 3 CWFS stars only. The performance of the different guide star modes used during the commissioning runs can be found in other presentations during this conference.[5,6] The commissioning of other guiding modes is still pending (1 CWFS and 3 ODGWs).

The GSAOI and the OT have been extensively tested since December 2011. The OT has been used to construct the GSAOI observations for selected commissioning targets, trigger the observations and observe the sequences through the sequence executor. During the tests several problems were encountered and fixed. The implementation of GSAOI in the OT and the inclusion of the MASCOT algorithm to search for CWFS and ODGW stars have been proved to be very robust. It is clear that more tests are required to complete this very important tool that will be used by our community in the future. The tests will continue during the second semester of 2012 when the GeMS/GSAOI commissioning is resumed.

7. CURRENT STATUS

In May 2012, the GSAOI has been removed from the telescope to the Instrument Laboratory for a general engineering maintenance. It is expected that GSAOI commissioning will be resumed at the end October 2012, after CANOPUS is installed back on the telescope. The call for the Science Verification of GeMs/GSAOI is expected to be released at the beginning of 2012B semester. The System Verification (SV) is the final step of testing prior to general use of any instrument by the Gemini community. There are two GeMS commissioning runs scheduled before the SV can be started at the end of the year.

ACKNOWLEDGMENTS

The Gemini Observatory is operated by the Association of Universities for Research in Astronomy, Inc., under a cooperative agreement with the NSF on behalf of the Gemini partnership: the National Science Foundation

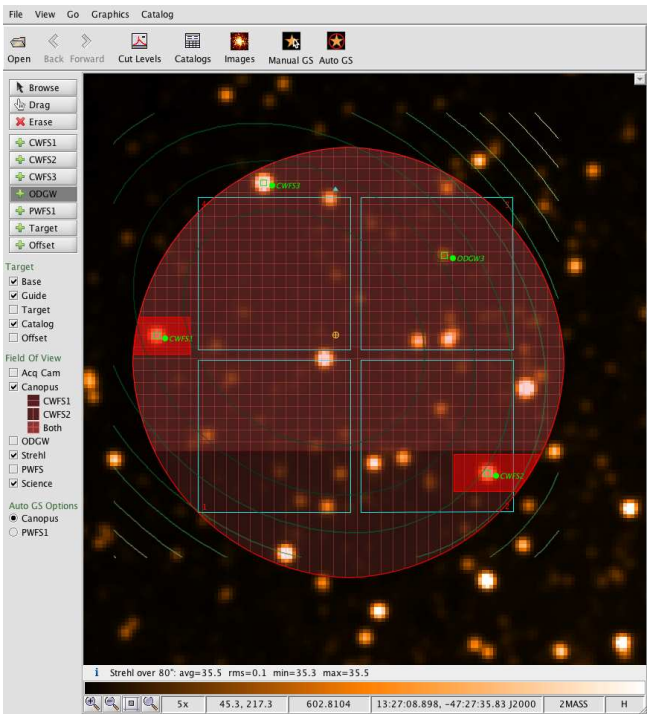

Figure 10. The OT position editor. The GSAOI detectors (cyan squares) and the CANOPUS patrol field area (red circle) are marked. The three CWFSs and the ODGW stars are represented by green squares. The Strehl map from the best asterism is superimposed as a green/yellow contours. The average, *rms*, minimum and maximum Strehl values are shown at the bottom of the position editor.

(United States), the Science and Technology Facilities Council (United Kingdom), the National Research Council (Canada), CONICYT (Chile), the Australian Research Council (Australia), Ministério da Ciência, Tecnologia e Inovação (Brazil) and Ministerio de Ciencia, Tecnología e Innovación Productiva (Argentina)

REFERENCES

[1] Neichel, B., Rigaut, F. and et al.,"The Gemini MCAO System GeMS: nearing the end of a lab-story", [*Adaptive Optics Systems II*], B. L. Ellerbroek, M. Hart, N. Hubin and P. L. Wizinowich, eds., *Proc. SPIE* **7736**, 7736-06 (2010).

[2] Rigaut, F., Neichel, B., Boccas, M., Bec, M., Garcia-Rissmann, A. and Gratadur, D., "A Sample of GeMS Calibrations and Control Schemes", in [*1st AO4ELT Conference - Adaptative Optics for Extremely Large Telescopes*], Clénet, Y., Conan, J.-M., Fusco, T. and Rousset, G., eds., **08001**, 1–6, EDP Sciences (ao4elt.edpsciences.org) (2010).

[3] Neichel, B., Rigaut, F., Bec, M. and Garcia-Rissmann, A., "Reconstruction Strategies for GeMS", in [*1st AO4ELT Conference - Adaptative Optics for Extremely Large Telescopes*], Clénet, Y., Conan, J.-M., Fusco, T. and Rousset, G., eds., **08001**, 1–6, EDP Sciences (ao4elt.edpsciences.org) (2010).

[4] D'Orgeville, C., Daruich, F., and et al., "The Gemini South MCAO Laser Guide Star Facility: getting ready for 1rst light", in [*Adaptive Optics Systems*], Hubin, N., Max, C., and Wizinowich, P., eds., *Proc. SPIE* **7015**, 70152P (2008).

[5] Rigaut, R., Neichel, B., Boccass, M. and et al.,"GeMS: first on-sky results", in [*Adaptive Optics Systems III*], Ellerbroek, B. L., Machetti, E. and Veran, J.-P., eds., *Proc. SPIE* **8447**, 8447-18 (2012).

[6] Neichel, B., Rigaut, F., Arriagada, G. and et al., "Status and performance of the Gemini MCAO System GeMS", in [*Adaptive Optics Systems III*], Ellerbroek, B. L., Machetti, E. and Veran, J.-P., eds., *Proc. SPIE* **8447**, 8447-32 (2012).

[7] McGregor, P., Hart, J., Stevanovic, D. and et al.,"Gemini South Adaptive Optic Imager (GSAOI)", in [*Ground-based instrumentation for Astrononomy*], Moorwood, F. M. and Iye, M. eds., *Proc. SPIE* **5492** 1033–1044 (2004).

[8] Rigaut, R., Neichel, B., et al.,"GeMS sees star light", in [*2nd AO4ELT Conference - Adaptative Optics for Extremely Large Telescopes*] **AO4ELT2** (2011) http://ao4elt2.lesia.obspm.fr/

[9] Fowler, A. M. and Gatley, I., "Demonstration of an algorithm for read-noise reduction in infrared arrays," *The Astrophysical Journal* **353**, L33 – L34 (1990).

[10] Young, P. L., McGregor, P., van Harmelen, J. and B. Neichel, "Using ODGWs with GSAOI: software and firmware implementation challenges", in [*Software and Cyberinfrastructure for Astronomy II*], Radziwill, N. M. and G. Chiozzi, G. eds., *Proc. SPIE* **8451**, 8451-77 (2012).

[11] http://www.gemini.edu/sciops/instruments/gcal/?q=sciops/instruments/gcal

[12] http://www.noao.edu/kpno/manuals/whirc/reports.html

[13] http://www.gemini.edu/node/11715

[14] Nikolaev, S.,Weinberg, M. D. and et al., "A Global Photometric Analysis of 2MASS Calibration Data", *The Astronomical Journal* **120**, 3340–3350 (2000).

[15] http://www.gemini.edu/sciops/instruments/gsaoi/itc-sensitivity-and-overheads?q=/node/11566

[16] Zacharias, N., Finch, C., Girard, T. and et al., "The Third US Naval Observatory CCD Astrograph Catalog (UCAC3)", *The Astronomical Journal* **139**, 2184 – 2199 (2010).

[17] Hayward, T.,"NICI World Coordinate System calibration", Gemini Internal Documentation, November (2011).

[18] http://www.gemini.edu/node/11161

[19] Nuñez, A. and Walker, S., "Automatic Validation of Science Programs in the Observing Tool", in [*Advance Software and Control for Astronomy II*], Bridger, A. and Radziwill, N. M. eds., *Proc.SPIE* **7019**, 701900S-1 – 701900S-9 (2008)

[20] Rigaut, F. and Neichel, B.,"MAsCOt: the Multi-Conjugate Adaptive Optic Tool", Gemini Internal Documentation, November (2010).